

Nanowatt-Level Photoactivated Gas Sensor Based on Fully-Integrated Visible MicroLED and Plasmonic Nanomaterials

Incheol Cho, Young Chul Sim, Kichul Lee, Minkyu Cho, Jaeho Park, Mingu Kang, Ki Soo Chang, Chan Bae Jeong, Yong-Hoon Cho,* and Inkyu Park*

Photoactivated gas sensors that are fully integrated with micro light-emitting diodes (μ LED) have shown great potential to substitute conventional micro/nano-electromechanical (M/NEMS) gas sensors owing to their low power consumption, high mechanical stability, and mass-producibility. Previous photoactivated gas sensors mostly have utilized ultra-violet (UV) light (250–400 nm) for activating high-bandgap metal oxides, although energy conversion efficiencies of gallium nitride (GaN) LEDs are maximized in the blue range (430–470 nm). This study presents a more advanced monolithic photoactivated gas sensor based on a nanowatt-level, ultra-low-power blue ($\lambda_{\text{peak}} = 435$ nm) μ LED platform (μ LP). To promote the blue light absorbance of the sensing material, plasmonic silver (Ag) nanoparticles (NPs) are uniformly coated on porous indium oxide (In_2O_3) thin films. By the plasmonic effect, Ag NPs absorb the blue light and spontaneously transfer excited hot electrons to the surface of In_2O_3 . Consequently, high external quantum efficiency (EQE, $\approx 17.3\%$) and sensor response ($\Delta R/R_0$ (%) = 1319%) to 1 ppm NO_2 gas can be achieved with a small power consumption of 63 nW. Therefore, it is highly expected to realize various practical applications of mobile gas sensors such as personal environmental monitoring devices, smart factories, farms, and home appliances.

1. Introduction

Nowadays, there are various emerging applications of mobile gas sensing technology combined with the internet of things (IoT) technology. For example, personalized gas alarm systems that can detect atmospheric pollutants or toxic fumes are one

of the most widely used applications. In addition, mobile gas monitoring is being widely applied in the manufacturing, agriculture, automotive, and healthcare industries. In order to meet these needs, gas sensing devices are required to be more sensitive, compact, simple to measure, and inexpensive. Primarily, it should consume electrical energy as low as possible to be combined in battery-driven or photovoltaic-powered mobile systems. Current low-power gas sensing technologies can be summarized as the following categories; 1) MEMS/NEMS (Micro/Nano-electro-mechanical systems)-based chemoresistive gas sensors,^[1–8] 2) nanoscale self-heated chemoresistive gas sensors,^[9–12] 3) room-temperature chemoresistive gas sensors,^[13–15] 4) self-powered piezoelectric/optical gas sensors,^[16–19] and 5) monolithic photoactivated chemoresistive gas sensors.^[20–22] Among them, monolithic photoactivated gas sensors have recently emerged and been spotlighted for their low power consumption, high sensitivity,


excellent stability, compact size, and mass-producibility. Monolithic photoactivated gas sensors are directly mounted on the light sources such as light emitting diodes (LED). Such sensors could significantly improve the light energy transfer efficiency by reducing the distance between the sensing material and the light source through flip-chip integration or direct surface integration. In our previous work, we introduced a highly miniaturized photoactivated gas sensor, integrated on a low-power ultra-violet (UV) micro-LED platform (μ LP).^[23] The peak wavelength of μ LPs was near UV region ($\lambda_{\text{peak}} = 390$ nm) to match with the absorption band of the sensing material (ZnO nanowire). Through miniaturization, our sensor showed a record low power consumption (≈ 187 μ W) and comparable sensing performance with previous chemoresistive gas sensors. However, theoretically, gallium nitride (GaN)-based LEDs show the highest energy conversion efficiency not in the ultraviolet but in the blue regime ($\lambda = 430$ – 450 nm). It has been demonstrated that the energy efficiency of GaN LEDs is lower at the shorter emission wavelengths, which is mainly caused by the poor quality and self-absorption of InGaN epi-layers of UV LEDs grown by the metal organic chemical vapor deposition (MOCVD) process.^[24]

In this paper, a highly energy-efficient photoactivated gas sensor based on the blue μ LP ($\lambda_{\text{peak}} = 435$ nm) is introduced to

I. Cho, K. Lee, M. Cho, J. Park, M. Kang, I. Park
Department of Mechanical Engineering
Korea Advanced Institute of Science and Technology (KAIST)
Daejeon 34141, Republic of Korea
E-mail: inkyu@kaist.ac.kr

Y. C. Sim, Y.-H. Cho
Department of Physics
Korea Advanced Institute of Science and Technology (KAIST)
Daejeon 34141, Republic of Korea
E-mail: yhc@kaist.ac.kr

K. S. Chang, C. B. Jeong
Center for Scientific Instrumentation
Korea Basic Science Institute
Daejeon 34133, Republic of Korea

 The ORCID identification number(s) for the author(s) of this article can be found under <https://doi.org/10.1002/smll.202207165>.

DOI: 10.1002/smll.202207165

dramatically reduce the power consumption for the sensor operation. **Figure 1a** shows the schematic illustration of the sensor structure. A semiconductor metal oxide (SMO) sensing material is irradiated from the bottom of the sensor platform where a μ LED is embedded. It has two p - n contact electrodes for operating the LED and two interdigitated electrodes for measuring the gas sensing signal. Meanwhile, further consideration about the coupling of the emission spectrum of LED and the light absorbance of SMOs is necessary. General wide-bandgap SMOs such as SnO_2 , In_2O_3 , ZnO , and TiO_2 have very low absorbance in the range of visible light (**Figure 1b-(i)**). In this study, silver (Ag) nanoparticles (NPs) were coated on the surface of SMOs to promote the photoactivation in the blue range. According to recent discoveries, plasmonic metal NPs can generate hot-electrons under photo-illumination.^[25] Following light absorption and localized surface plasmon resonance (LSPR) excitation in the metal NPs, electromagnetic decay takes place on a femto-second timescale, either radiatively through re-emitted photons or non-radiatively by transferring the energy to hot electrons.^[26] Hot electrons with energies higher than the Schottky barrier energy (ϕ_{SB}) can be injected into the SMO. Here, the energy

needed for hot electrons to overcome the energy barrier is considerably smaller than the bandgap (E_g) of SMOs.^[27–28] Especially, Ag NPs show very high optical extinction at the blue light (430–460 nm) among various plasmonic metal NPs. Lastly, In_2O_3 (electron affinity, $\chi \approx 5$ eV), which has a low junction barrier with Ag (work function, $\phi_m \approx 4.26$ – 4.74 eV), is utilized as a gas-sensing material (**Figure 1b-(ii)**). Porous In_2O_3 films were prepared through a wafer-scale, vacuum physical-vapor-deposition method (i.e., sputtering with a high-purity material source) and uniformly decorated by Ag NPs through the e-beam evaporation process. In particular, glancing angle deposition (GLAD) technique was utilized for the deposition of porous nanocolumnar metal oxides. GLAD is a technique where the direction of vapor flux impinging on a substrate is inclined.^[29] By the nanoscale shadowing effect, porous, columnar, and granular metal oxide films can be formed. This paper comprehensively investigates the light-emitting performance, sensing performance of the fabricated sensor, and the effect of Ag NPs. As consequence, a high external quantum efficiency (EQE, $\approx 17.3\%$) and a high sensor response ($\Delta R/R_0$ (%) = 1319%) to 1 ppm NO_2 gas with a power consumption of 63 nW could be achieved.

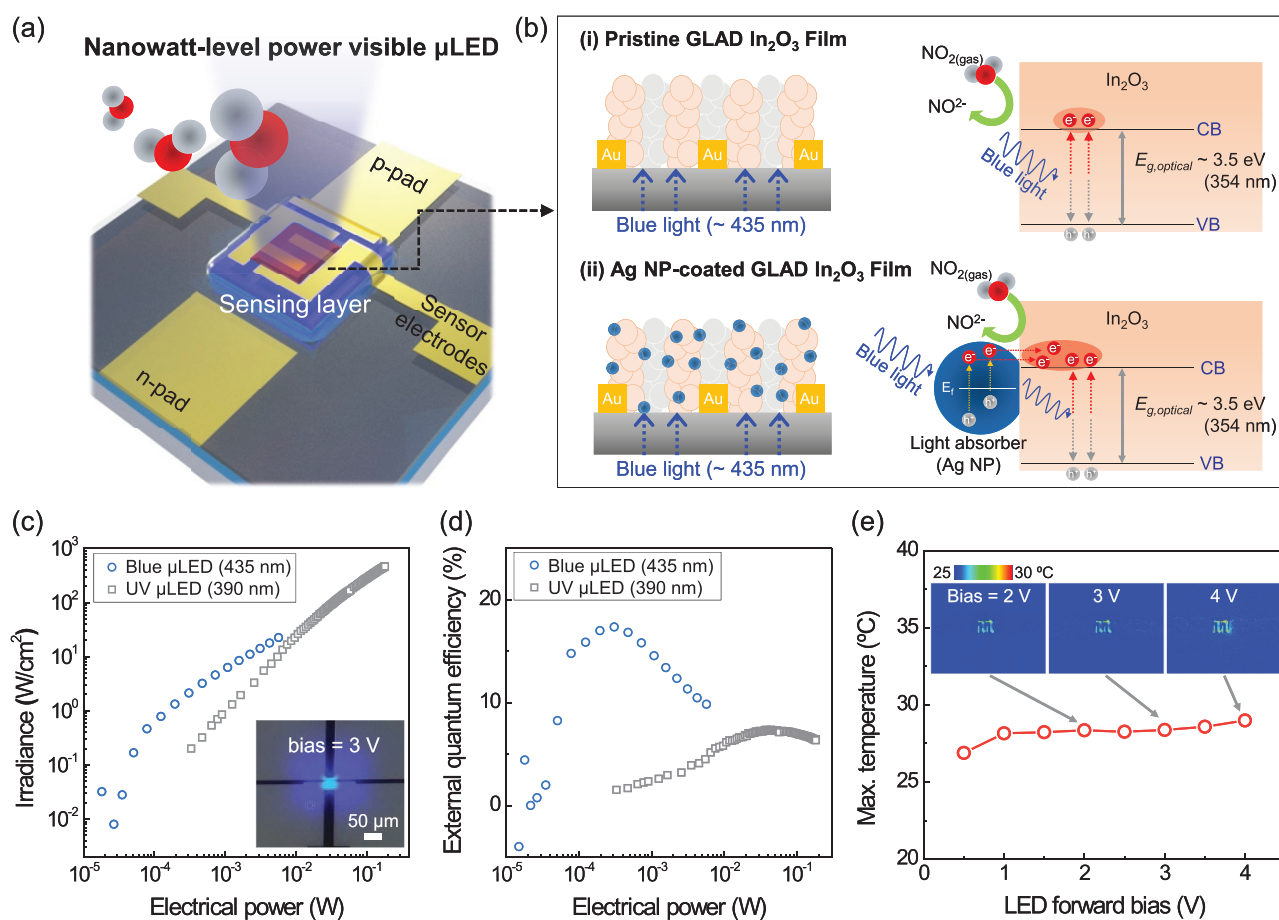


Figure 1. a) Schematic illustrations of a blue μ LED-based gas sensor. b) An electronic band structure of (i) a pristine In_2O_3 and (ii) an Ag NP- In_2O_3 junction under blue light illumination. Comparison of c) irradiance (W/cm^2) and d) external quantum efficiency (%) between fabricated blue and UV μ LEDs depending on the input electrical power. An inset image in (c) shows a blue-emitting LED with forward bias = 3 V. e) Temperature mapping of the fabricated blue μ LP with different forward bias (2, 3, and 4 V) and maximum temperatures on the mapping image according to the LED forward bias (0.5–4 V).

2. Results and Discussion

2.1. Energy Efficiency of the Fabricated μ LP

The light–current–voltage (I – V) measurements were performed to evaluate the electrical and optical properties of fabricated blue μ LPs (Figure 1c–e). In Figure S1a,b (Supporting Information), the electrical power densities of blue μ LP were obtained by measuring the I – V characteristics with a forward voltage ranging from 0 to 4 V. Turn-on voltage was measured ≈ 2 V. Also, the irradiance (W cm^{-2}) of the blue μ LP was obtained by the electroluminescence measurement. Irradiances of the blue μ LP are higher than those of the UV μ LP in Figure 1c at the low power range (sub-milliwatt). The inset image in Figure 1c shows the illuminating μ LP by applying a forward bias of 3.0 V. Blue emission of the fabricated μ LP can be visually confirmed. Furthermore, the maximum EQE of blue μ LP is $\approx 17.4\%$, which is 2.38 times higher than that of UV μ LP (7.3%), as shown in Figure 1d. As mentioned before, these improvements in blue μ LEDs are majorly attributed to the high-quality epi-layers of MOCVD GaN.

In addition to the light intensity, the sensing performance of SMO gas sensors is also influenced by the temperature of sensing materials. It was reported that the temperature near the p -contact edge of the LED rises at high current densities due to the local self-heating by the current crowding effect.^[30] Therefore, the surface temperature of the μ LP was analyzed to ensure the validity of evaluations of gas-sensing performance. In order to obtain the temperature map on the surface of μ LPs, an infrared micro-thermography system was utilized. Detailed measurement processes are explained in the section of Measurement of the surface temperature of the μ LP in (Figure S2, Supporting Information). Figure S3 (Supporting Information) shows the temperature map of the μ LP applied with different forward biases (0.5–4 V). From this result, it can be observed that the temperature change on the surface of the μ LP is negligible at the operating voltages. In addition, it can be confirmed that the local temperature rise at the p -contact edge also rarely occurs. Figure 1e shows the summarized maximum temperature of the μ LP with different forward biases (0.5–4 V). The maximum temperature change (ΔT_{max}) is ≈ 4 °C at a forward bias of 4 V. Therefore, the fabricated μ LP effectively dissipates generated heat, and the gas sensing performance is not influenced by the local heat generation of the μ LP.

2.2. The Optical Absorbance of Sensing Materials

Figure 2a shows the emission spectrum of the fabricated blue μ LP and the absorption spectrum of GLAD In_2O_3 . The measured peak emission wavelength (λ_{peak}) of the fabricated blue μ LP is 435 nm. However, the optical bandgap of In_2O_3 is 3.5 eV which corresponds to the photon energy of $\lambda = 354$ nm.^[31] Therefore, the absorption band of GLAD In_2O_3 is rarely overlapped with the emission spectrum of blue μ LP. On the other hand, Figure 2b shows the photo-absorbance spectra of various metal NPs (Ag, Au, and Pt) deposited on transparent quartz substrates. Identical to Ag NPs, the other metals were also deposited with a thickness of 1.5 nm by e-beam evaporation.

LSPR peak wavelength of 1.5 nm-thick Ag NPs is 433 nm, well matching with the peak emission wavelength (435 nm) of the fabricated blue μ LP. Meanwhile, Au NPs, also known to exhibit an excellent plasmonic property, show LSPR peak wavelength at 620 nm. Pt NPs, one of the representative chemical catalysts for SMO gas sensors, rarely show the LSPR effect in all analyzed wavelength regime.

Figure 2c–e shows the SEM images, size distributions, and absorbance spectra of various sized plasmonic Ag NPs (1, 1.5, and 2 nm-thick) deposited on a quartz substrate. Peak diameters of 1, 1.5, and 2 nm-thick Ag NPs are 11.7 (full width at half maximum (FWHM) = 11.1 nm), 14.6 (FWHM = 10.9 nm), and 17.8 nm (FWHM = 13.5 nm), respectively. It can be confirmed that the size distributions of NPs become larger and broader by increasing the deposition thickness. Figure 2e shows that LSPR peak wavelengths of 1, 1.5, and 2 nm-thick Ag NPs are 422, 433, and 440 nm, respectively. Therefore, 1.5 nm-thick Ag NPs showed the highest concordance with the emission wavelength (435 nm) of the fabricated blue μ LP. In addition, 1.5 and 2 nm-thick Ag NPs show 31.5% and 79% higher peak-absorbance, respectively, than that of 1 nm-thick Ag NPs. These peak-shift and broadening of absorbance spectra are attributed to the size-dependent LSPR characteristics and electron-boundary scattering at the surface of Ag NPs. Since 2 nm-thick NPs pose a risk of electrical connection between the surface electrodes, In_2O_3 was finally coated with 1.5 nm-thick Ag NPs. Figure S4 (Supporting Information) shows 3D surface morphologies of the bare Si substrate and e-beam evaporated Ag NPs (deposition thickness = 1.5 nm) on the Si surface measured by an atomic force microscope. It can be seen that the shape of silver NPs on the Si substrate is quasi-hemispherical. The average peak height of Ag NPs is ≈ 10.93 nm. According to literature, when the dimension of plasmonic NPs is comparable to or smaller than the electronic mean free path (≈ 53.3 nm for bulk silver^[32]) and there are adsorbates on the NPs, the dephasing mechanism for LSPR, such as chemical interface damping, may dominate.^[33] In this direct electron injection mechanism, the interaction of LSPR with adsorbates induces direct excitation of resonant electrons into the unoccupied states of adsorbates. However, the interfacial electronic structure between plasmonic NPs and semiconductors is still being explored, and further experimental and theoretical studies will be required for more rigid understanding in the future. Conclusively, it is expected that emitted photons from the blue μ LP can efficiently induce plasmonic excitation of Ag NPs and promote photoactivation at the surface of In_2O_3 .

2.3. Results of Sensor Fabrication

Figure 2f shows the optical microscope images of pristine In_2O_3 and Ag NP-coated In_2O_3 integrated on μ LPs, respectively. Due to the blue-absorption by plasmonic Ag NPs, the Ag NP-coated In_2O_3 film looks more reddish than the pristine In_2O_3 film. Figure 2g shows the cross-sectional transmission electron microscope (TEM) and top-view scanning electron microscope (SEM, inset) images of Ag NP-coated In_2O_3 film deposited on a plain silicon substrate. Columnar and granular nanostructure of GLAD In_2O_3 can be observed in the cross-sectional TEM image. The averages (standard deviation) of widths and heights

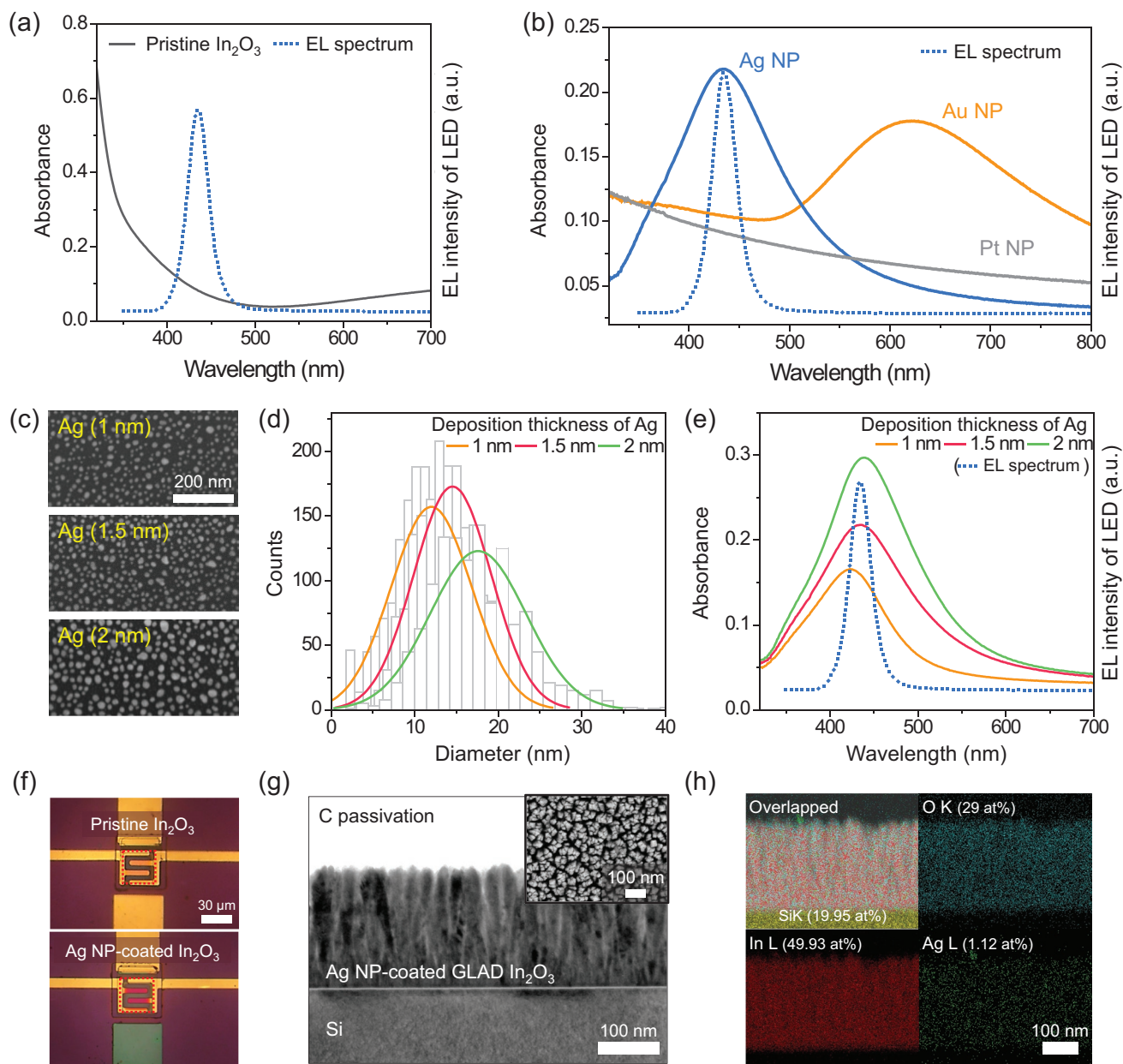


Figure 2. a) Electroluminescence (EL) spectrum of the fabricated blue GaN μ LED platform (μ LP) and absorbance spectrum of the pristine GLAD In_2O_3 . b) Absorbance spectrum of e-beam evaporated Ag, Au, and Pt NPs (thickness = 1.5 nm). c) SEM images, d) size distribution, and e) absorbance spectra of Ag NPs with various deposition thicknesses (1, 1.5, and 2 nm). f) Optical microscopic images of pristine GLAD In_2O_3 and Ag (1.5 nm) NPs-coated GLAD In_2O_3 integrated on μ LPs. g) Cross-sectional TEM image and h) TEM-EDS elemental mapping images of a FIB-milled Ag NPs-coated In_2O_3 film. An inset image in (g) is a top-view SEM image of nano-porous Ag NPs-coated In_2O_3 film.

of those nano-columns are 49.7 nm (\pm 7.4 nm) and 177 nm (\pm 9.8 nm), respectively. In the top-view SEM image, nano-sized gaps are uniformly distributed on the entire observed area. These nanogaps facilitate target gas molecules to diffuse to the depth-wise direction of the sensing film and provide larger surface area for the reaction with target gas.

In addition, Figure 2h shows the TEM-energy dispersive spectroscopy (EDS) elemental mapping images of the cross-section of the Ag NP-coated In_2O_3 film. It can be confirmed that the deposited Ag NPs (Ag L, 1.12 At%) penetrated well through the nanogaps and were uniformly distributed in the upper and

lower regions of the In_2O_3 film. Figure S5 (Supporting Information) shows the X-ray photoelectron spectroscopy (XPS) spectra of Ag NPs (1.5 nm)-coated In_2O_3 . Clear peaks of Ag (Ag $3d_{3/2}$ and Ag $3d_{5/2}$), O (O 1s), and In (In $3d_{3/2}$ and In $3d_{5/2}$) indicate that Ag NPs were well coated on the In_2O_3 film, and there was no chemical transition during the Ag-deposition process.

2.4. Effect of Plasmonic Excitation

Gas sensing tests of the fabricated sensors were conducted with nitrogen dioxide (NO_2) gas to evaluate the effects of the surface

metal decoration. The noble metal decoration on the surface of SMOs generally affects the sensor response via plasmonic excitations as well as chemical catalytic effects. In order to verify the dominant effect, a sample of Pt-NP-coated In_2O_3 was also prepared as a comparison group. Pt NP is a well-known representative surface sensitizer of SMO gas sensors but has no LSPR under light illumination, as seen in Figure 2b. Therefore, any response improvements of Pt-NP-coated In_2O_3 under light illumination may be attributed purely to the chemical catalytic effect of Pt NPs. **Figure 3a,b** shows the responses of monolithic photoactivated gas sensors with pristine In_2O_3 and Ag NP-coated In_2O_3 on blue (435 nm) μLPs to 1 ppm NO_2 gas under increasing LED operating power. Figure S6a,b

(Supporting Information) shows Pt NP-coated In_2O_3 on a blue μLP and pristine In_2O_3 on a UV (390 nm) μLP to 1 ppm NO_2 gas under increasing LED operating power. Here, the sample of pristine In_2O_3 on a UV (390 nm) μLP was prepared to compare previously developed UV μLPs and the proposed blue μLPs . The base resistance of all sensors in the pure air (R_0) decreased by increasing the operating power of μLED because of the generation of photoelectrons. The resistance of n-type In_2O_3 increases under NO_2 exposure because of surface depletion by electron transfer from metal oxides to surface oxygen. The normalized responses [$\Delta R/R_0 \times 100$ (%), $\Delta R = R - R_0$] of all sensors according to the applied μLED power are summarized in Figure 3c. Normalized responses of each sensor

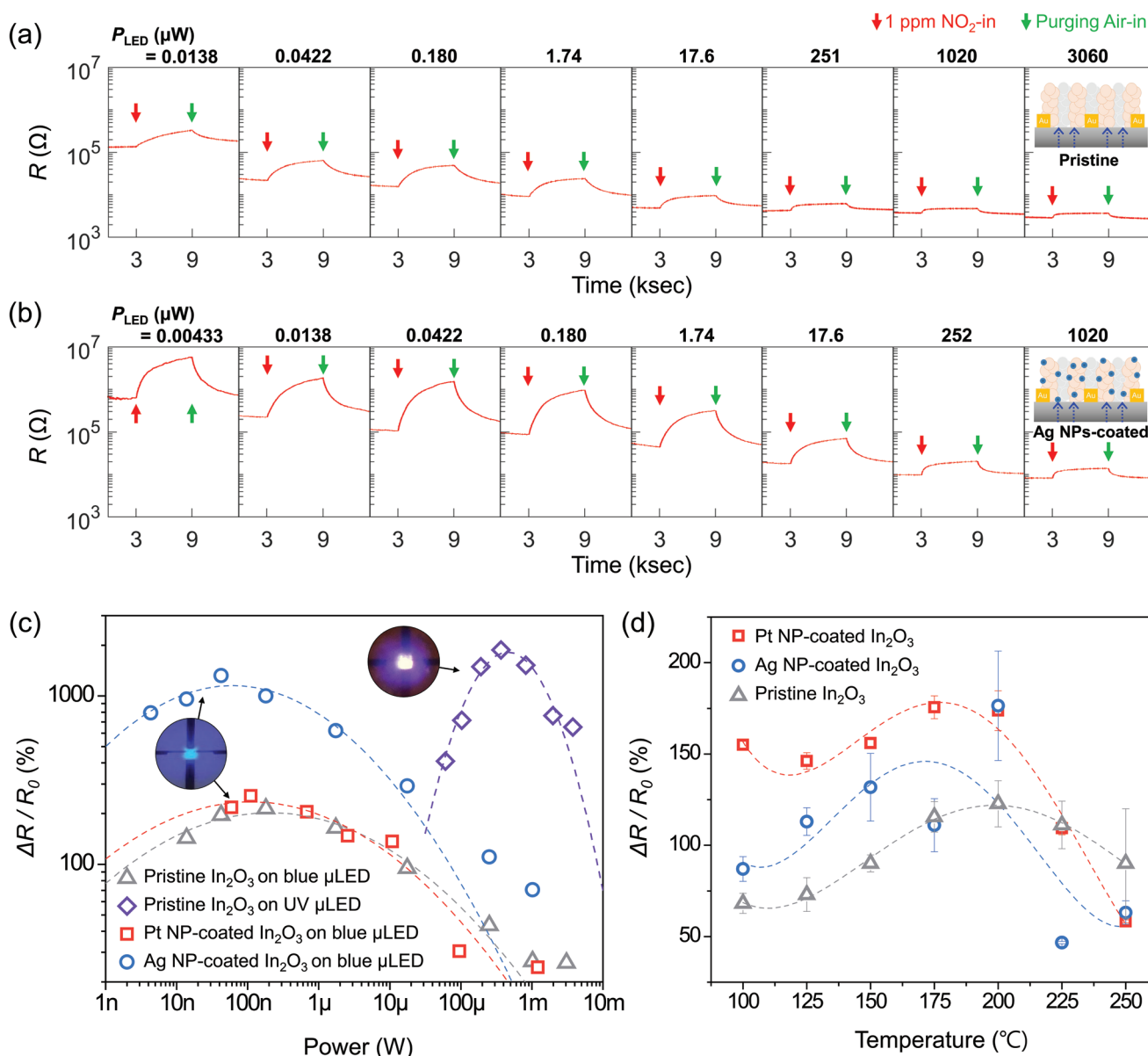


Figure 3. Responses of monolithic photoactivated gas sensors to 1 ppm NO_2 gas under different input electrical powers: a) pristine In_2O_3 and b) Ag NPs-coated In_2O_3 on blue (435 nm) μLPs . c) Summary of normalized responses [$\Delta R/R_0 \times 100$ (%)] of Pt NPs-coated In_2O_3 and Ag NPs-coated In_2O_3 on blue μLPs . The plot also includes the normalized responses of pristine In_2O_3 sensors on a blue and UV μLPs for comparison. d) Summary of normalized sensor response ($\Delta R/R_0$) to 1 ppm NO_2 gas at different temperatures (100–250 $^{\circ}\text{C}$).

showed bell-shaped tendencies as in previous works.^[23] Data points were fitted to the log-normal distribution function, $f(x) = \frac{1}{x\sigma\sqrt{2\pi}} \exp\left(-\frac{(\ln x - \mu)^2}{2\sigma^2}\right)$. The optimal operating power where the response is maximum [i.e., peak mode defined as $\exp(\mu - \sigma^2)$] for pristine In_2O_3 on a UV μLP (461 μW) is 2305 and 4610 times higher than those of pristine In_2O_3 (0.2 μW) and Pt-NP-coated In_2O_3 (0.1 μW) on blue μLP s, respectively. However, in terms of response, pristine In_2O_3 on a UV μLP shows much higher response ($\Delta R/R_0 = 1820\%$) compared to pristine In_2O_3 on blue μLP s ($\Delta R/R_0 = 214\%$) at the optimal power. This is because the photons emitted from the blue μLP have insufficient energy (≈ 2.86 eV) to generate photoelectrons in In_2O_3 (the optical bandgap ≈ 3.5 eV). In addition, Pt-NP-coated In_2O_3 exhibits a minor improvement in response (255%) compared to the pristine In_2O_3 , which means that Pt NPs rarely promote the absorption of blue light and surface activation of the sensing material. On the other hand, Ag NP-coated In_2O_3 on the blue μLP exhibits 616% improvement in the peak sensor response ($\Delta R/R_0 = 1319\%$) compared to pristine In_2O_3 at the optimal operating power (63 nW). It is because the Ag NPs facilitate the generation of excited electrons under blue light illumination, and the photoelectrons, which propagate to the surface of In_2O_3 , actively promote the gas reactions. In conclusion, the degraded sensor response of In_2O_3 in the blue range can be effectively overcome by coating with Ag NPs that induce LSPR effects. Furthermore, optimal operating power (63 nW) of the proposed gas sensor integrated on the blue μLP is the record lowest power consumption among those of all the reported gas sensors, including NEMS/MEMS heating platforms and photoactivation platforms.^[1–12,20–23]

As mentioned before, the noble metal decoration on the surface of SMOs may enhance the sensor response via chemical catalytic effect or plasmonic excitation under light illumination. In terms of chemical catalysts, the noble metals promote the dissociation of gas molecules and provide a lower energy path for the adsorption of gas analytes and diffusion onto the surface of supporting metal oxides, thereby enhancing the reaction between gas analytes and metal oxides. It is called the “spill-over effect” of noble metal catalysts.^[34] In order to verify the dominating factor between plasmonic excitations and chemical catalytic effects, responses of pristine In_2O_3 , Pt-NP-coated In_2O_3 , and Ag NP-coated In_2O_3 were compared in the high-temperature heating condition. In addition, tests were conducted in dark conditions to eliminate any effects of photons. Figure S7a–c (Supporting Information) shows normalized sensor responses [$\Delta R/R_0 \times 100$ (%)] of pristine In_2O_3 , Ag NP-coated In_2O_3 , and Pt-NP-coated In_2O_3 , respectively, to 1 ppm NO_2 gas at various temperatures (100–250 °C with an interval of 25 °C). The samples were exposed to 1 ppm NO_2 gas repeatedly three times under each temperature condition. Figure 3d shows an averaged sensor response ($\Delta R/R_0$) to 1 ppm NO_2 gas depending on heating temperatures. Similar to light illumination, sensor responses also follow bell-shape tendency as increasing temperatures by balancing between decreasing surface densities and increasing surface reactivities of adsorbed oxygen ions.^[35–37] In contrast to the results in Figure 3c, Pt-NP-coated In_2O_3 exhibits the highest response

(maximum $\Delta R/R_0 = 178\%$) in most of temperature range, followed by Ag NP-coated In_2O_3 and pristine In_2O_3 (maximum $\Delta R/R_0 = 145$ and 121%, respectively). From this result, it can be concluded that the chemical catalytic effect is more significant with Pt NPs than with Ag NPs. On the other hand, the huge response improvement of Ag NP-coated In_2O_3 seen in Figure 3c was influenced dominantly by the effect of plasmonic excitation under blue-light illumination than by the chemical catalytic effect. Gas tests were also conducted on representative volatile organic compounds (VOC) gases such as acetone, ethanol, carbon monoxide, and methanol with Ag NP-coated In_2O_3 on blue μLP (Figure S8, Supporting Information). Since they are reducing gases, they donate free electron carriers on the surface of n-type In_2O_3 , lowering the electrical resistance. It was observed that blue μLP does not have a good selectivity to NO_2 gas against other reducing gases. Although it is difficult to selectively discriminate the target gas only with the steady-state response (R/R_0), it is possible to develop an electronic nose system by applying the deep learning-based pattern recognition since each gas shows a unique transient response. In the present study, it should be noted that we have focused on verifying the performance of the nanowatts-level ultra-low-power μLED gas sensor platform, and in-depth verification of novel sensing materials, not on developing a selective gas sensor for a particular target gas.

2.5. Sensing Performances

Further NO_2 gas tests with Ag NP-coated In_2O_3 on blue μLP s to evaluate the lower limitation of detection and the response time. Tests were conducted with two modes of operating power (0.11 and 676 μW). The low-power mode of 0.11 μW is near the optimal operating power where the sensor response is maximized. Similar to the previous reports, the response speed of photoactivated gas sensors is accelerated by increasing the light intensity.^[38] Therefore, the high-power mode (676 μW) was individually tested for the high-speed response. Figure 4a shows the resistance change of the sensor to NO_2 gas with concentrations ranging from 0.25 to 5 ppm. Results to the lower NO_2 concentration range from 0.14 to 0.25 ppm are shown in Figure 4b. The result shows clear response and recovery over the wide concentration range of NO_2 gas. The baseline sensor resistance was overall higher in the low-power mode due to the small photocurrent generation. For a more accurate evaluation, the noise level of measurement was calculated at the baseline signal. The maximum baseline noise level ($3N_{\text{max}}$) was 3.88%. The limit of detection (LOD) can be determined at the point where the signal is three times larger than the maximum noise level ($3N_{\text{max}}$).^[39] Figure 4c is the calibration graph of the normalized sensor response [$\Delta R/R_0 \times 100$ (%)] to NO_2 concentrations. The sensor responses have good linearity in the log–log scale plot [$\log_{10}(\Delta R/R_0) = 1.726 \times \log_{10}(P) + 3.249$, $r^2 = 0.999$ for the low-power mode and $\log_{10}(\Delta R/R_0) = 1.352 \times \log_{10}(P) + 2.279$, $r^2 = 0.998$ for the high-power mode, where P is the NO_2 concentration (ppm)]. The extrapolated line met $3N_{\text{max}}$ at NO_2 concentrations of 28.8 and 56.2 ppb for the low and high-power modes, respectively. Therefore, more improved LOD

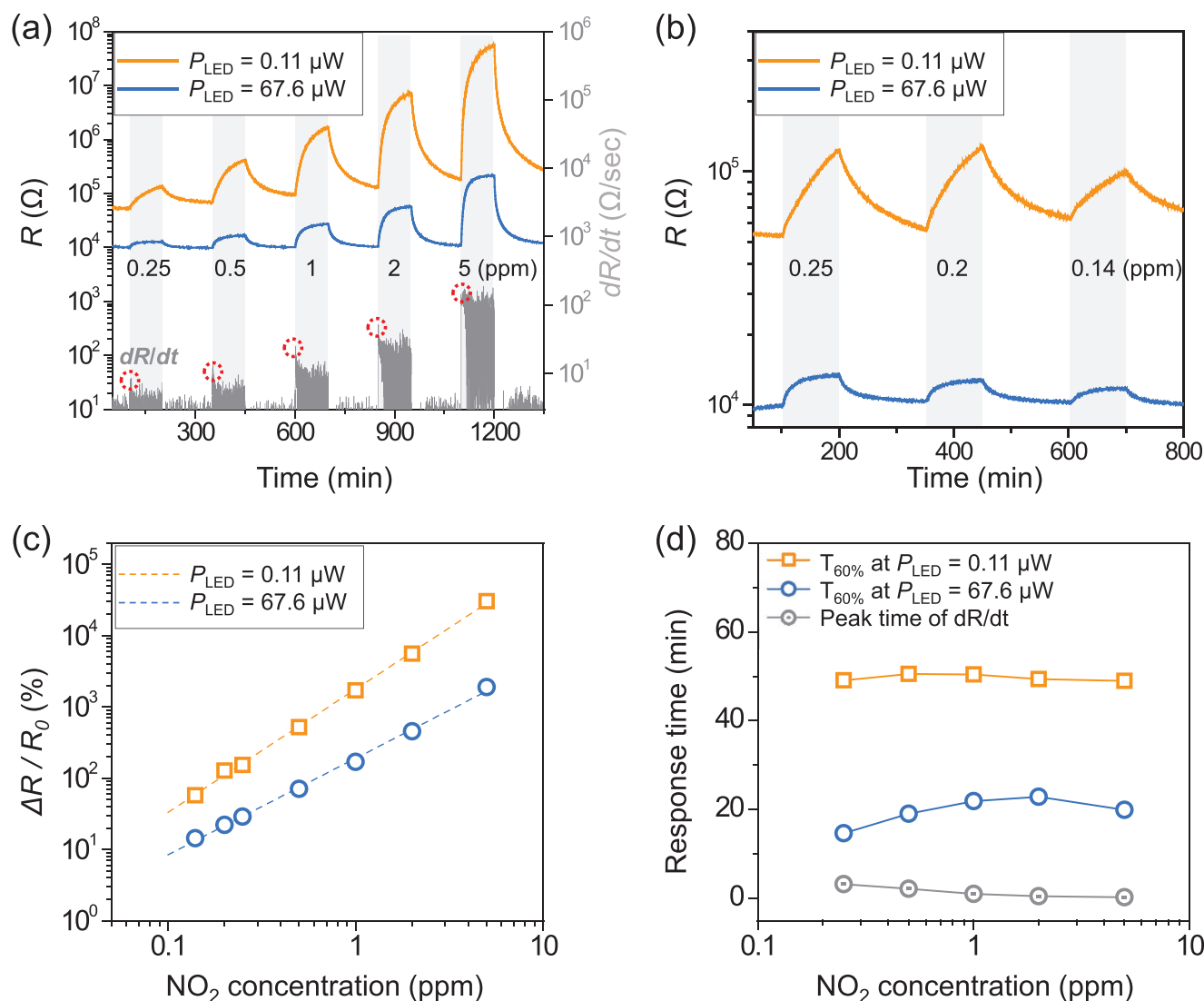


Figure 4. Nitrogen dioxide (NO₂) sensing performance of the monolithic photoactivated gas sensor (Ag NPs-coated In₂O₃ on a blue μLP) in two modes of operation power (0.11 and 67.6 μW). Dynamic response a) to 0.25–5 ppm and b) 0.14–0.25 ppm of NO₂ gas. c) Calibration graph of normalized sensor response [$\Delta R/R_0 \times 100$ (%) to NO₂ concentrations. d) Response time ($T_{60\%}$) to NO₂ concentrations.

(28.8 ppb) can be expected in the low-power mode. Figure 4d shows the response time ($T_{60\%}$) for low and high-power modes. The response time of the low-power mode ranges from 48 to 50 min which are 2.2–3.6 times larger than that of the high-power mode (15 to 22 min). In addition, time derivatives of dynamic sensor response when the μLED power is 67.6 μW shows peaks at the early-stage of gas exposure (i.e., the first peak where dR/dt is larger than 5 dB than at the normal state) as shown in Figure 4a. Monitoring these peaks enables rapid NO₂ detection less than 1 min (Figure 4d). Therefore, the monolithic photoactivated gas sensor can be operated in different power modes according to the adequate application target, such as lower concentration detection or faster sensor response. Table 1 summarizes the performances and power consumptions of low-power SMO-type gas sensor studies published so far. The joule heating method minimized the heating area by

fabricating microheaters and nanowire heaters with MEMS/NEMS technology to reduce power consumption, but the power consumption was still high on the milli-watts scale.^[4,8,42,43] Self-heating SnO₂ nanowire lowered the power consumption to μW -scale (continuous mode), but still failed to lower it to nano-watts scale, and its mechanical/thermal stability is very vulnerable due to its sensor structure in which a single nanowire is suspended.^[9] Recently, photoactivated gas sensors integrated with various light activation sources such as optical fibers, mini LEDs, and micro LEDs have been introduced.^[20–23,40–41] The suggested blue μLP -based sensor exhibits a record of low power consumption (63 nW) and excellent NO₂ sensing performance compared with previous works, including UV μLP -based gas sensors. Also, μLP -based sensors have excellent stability compared to heater-based sensors. Detailed explanation and stability tests are in the section of Excellent stability of the blue μLP in

Table 1. Summary of chemiresistive SMO-type gas sensors with various activation sources (MEMS/NEMS-based heater, self-heating nanowires, optical fiber, mini LED, and μ LED).

Sensing material	Activation source integration type (active area)	Detection gas (Dynamic range)	Working temperature	Power consumption	Sensitivity (R_a/R_g or R_g/R_a)
SnO ₂ NT [4]	Micro-heater surface integration ($3 \times 110 \mu\text{m}^2$)	H ₂ S (1–20 ppm)	220 °C	5 mW	3.8–11.6
WO ₃ NW [42]	Micro-heater surface integration ($50 \times 50 \mu\text{m}^2$)	NO ₂ (0.5–5 ppm)	250 °C	11 mW	1.1–3.3
ZnO NW [8]	Carbon NW heater Integration on carbon NW ($0.05 \times 0.05 \times 2 \mu\text{m}^3$)	NO ₂ (0.1–1 ppm)	200 °C	0.85 mW	2.5–40
ZnO NW [43]	Au NW heater Integration on Au NW ($0.25 \times 0.5 \times 60 \mu\text{m}^3$)	NO ₂ (0.05–2 ppm)	226 °C	1.62 mW	1.47–4.5
SnO ₂ NW [9]	Self-heating SnO ₂ NW ($0.06 \times 0.06 \times 1.85 \mu\text{m}^3$)	NO ₂ (0.1 ppm)	Self-heating (= 250 °C)	1.6 μ W	2
ZnO NW [40]	365 nm optical fiber Integration on fiber ($0.33 \times 100 \mu\text{m}^2$) (N.Q.)	Ethanol (0.01–0.5 ppm)	Global heating (300 °C)	120 mW	1.1–1.4
ZnO NR [41]	367 nm LED integration on package (N.Q.)	Ethanol (100–1000 ppm)	R.T.	608 mW	1.08–1.42
In ₂ O ₃ NP [20]	400 nm LED flip-chip integration ($0.1 \times 15 \text{ mm}^2$)	Ozone (38–726 ppb)	R.T.	0.25 mW	1.3–1.5
ZnO NR [22]	280 nm mini LED flip-chip integration ($750 \times 750 \mu\text{m}^2$)	NO ₂ (0.1–0.5 ppb)	R.T.	3 mW	2.18–5.33
ZnO NP [21]	455 nm mini LED surface integration ($190 \times 250 \mu\text{m}^2$)	NO ₂ (0.025–1 ppm)	R.T.	200 μ W for 0.25 ppm 300 μ W for 1 ppm	1.8–13.3
ZnO NW [23]	390 nm μ LED surface integration ($30 \times 30 \mu\text{m}^2$)	NO ₂ (0.06–2 ppm)	R.T.	184 μ W for 1 ppm	1.42–10.9
Ag NPs-coated-In ₂ O ₃ (This work)	435 nm μ LED surface integration ($50 \times 50 \mu\text{m}^2$)	NO ₂ (0.14–5 ppm)	R.T.	63 nW for 1 ppm	1.58–59.73

*Abbreviations: R.T. = Room temperature, N.Q. = Not quantified, NT = Nanotube, NW = Nanowire, NR = Nanorod, NP = Nanoparticle.

Supplementary information (Figure S9, Supporting Information). The blue μ LP operated stably without any change in LED characteristics even under accelerated testing conditions (turn-on power: 68 mW, pulse operation), and no sensor drift occurred even for a long period of about 44 h. The outstanding performance is comprehensively attributed to the excellent stability of GaN-based LED, miniaturization of the light source, direct surface integration of the sensing material, and utilization of the visible light region and plasmonic light absorber.

3. Conclusion

In this paper, monolithic photoactivated gas sensors based on a blue μ LED platform ($\lambda_{\text{peak}} = 435 \text{ nm}$), known to have the highest

energy conversion efficiency in gallium nitride (GaN) LEDs, were developed. The maximum EQE of the blue μ LED was highly improved to $\approx 17.3\%$, which is 2.74 times higher than that of the previous UV μ LED. In addition, we demonstrated that highly porous In₂O₃ films coated with Ag NPs could be effectively activated by the blue light. By the LSPR effect, emitted photons from blue μ LEDs could induce plasmonic excitation of Ag NPs very efficiently and promote the photoactivation at the surface of In₂O₃. By checking various coating thicknesses of Ag NPs, we found conditions in which the emission wavelength of blue LED (435 nm) and the LSPR peak of Ag NPs (433 nm) matched well, and the gas response improvement effect was maximized. This shows the possibility of maximizing the efficiency of the light source used in photoactivated gas sensing by tuning the size of the metal NPs. Furthermore, the plasmonic

excitation and chemical catalytic effect of Ag NPs are comprehensively studied by comparison with pristine In_2O_3 and Pt-NP-coated In_2O_3 . Conclusively, sensitivity-loss by blue-shifting ($\Delta R/R_0 = 1820\%$ with UV μLEDs , 214% with blue μLEDs to 1 ppm NO_2) could be effectively overcome by coating with Ag NPs ($\Delta R/R_0 = 1319\%$ with Ag NP-coated In_2O_3). The suggested technology will facilitate practical applications such as environmental monitoring, disease diagnosis, food process monitoring and agricultural fields by taking advantages of its extremely low power consumption and excellent sensing performances.

4. Experimental Section

Fabrication of Blue GaN MicroLEDs: The whole fabrication process is graphically illustrated in Figure S10 (Supporting Information). A μLP had two p - n contact electrodes for operating the LED and two interdigitated or parallel electrodes for measuring the gas sensing signal. The emission area of the μLP was $50 \times 50 \mu\text{m}^2$. Most of the process steps followed the previous work, which introduced the UV μLP .^[23] Exceptionally, the indium concentration of the InGaIn/GaN multi-quantum well (MQW) layer was precisely tuned for the blue-emission (i.e., emission wavelength 435 nm). In addition, the pyramidal patterned sapphire substrate (PSS) was utilized for the improved light-extraction efficiency for suppressing the light loss by the total internal reflections at the interface between GaN and sapphire substrate.

Glancing Angle Deposition of Porous Metal Oxide Films: Before integrating the sensing material, $3.5 \mu\text{m}$ -thick photoresist (AZ nlof 2035, MicroChemicals, Germany) was patterned on pre-fabricated blue μLPs to define a sensing area. Porous In_2O_3 films were integrated through the glancing angle deposition (GLAD) with a radio frequency (RF) sputtering system as illustrated in Figure S11 (Supporting Information). Specific process conditions of RF sputtering are as follow; 4 mTorr of argon atmosphere, tilting angle $= 85^\circ$, rotation speed $= 3.6 \text{ rpm}$, RF power $= 250 \text{ W}$, deposition time $= 90 \text{ min}$ ($30 + 30 + 30 \text{ min}$ with 10 min of cooling interval). Then, GLAD In_2O_3 films were lifted off in acetone. Finally, Ag NPs were coated on an entire sensor chip through an e-beam evaporation process. Their target thickness and deposition rate were set as 1.5 nm and 0.1 \AA s^{-1} , respectively, in a deposition monitoring system with a quartz crystal microbalance (QCM).

Optical Characterizations: The optical and electrical properties of blue μLPs were obtained using the L - I - V measurement system (OPI 160, WITHLIGHT, Korea) with an integrating sphere and a source meter (Keithley 2400, USA). The emission spectrum was also obtained by the same measurement setup with a constant input voltage. In order to analyze the photon absorbance of GLAD In_2O_3 film and metal NPs (Ag, Au, and Pt), they were deposited on transparent quartz pieces, and an absorbance spectrum was measured with the UV-vis spectrophotometer (Lambda 1050, PerkinElmer, USA) with an integrating sphere.

Material Characterizations: 3D surface morphologies of Ag NPs were measured with an atomic force microscope (XE-100, Park Systems, Korea). The micro/nanostructures of the Ag NP-coated In_2O_3 film were observed by a field emission scanning electron microscopy [FE-SEM (SU8230), Hitachi, Japan]. In addition, the cross-section of Ag NP-coated In_2O_3 film was prepared by using focused ion beam (FIB) milling (Dual-beam FIB system, FEI, USA) and was observed by ultra-high-resolution SEM [UHR-SEM (SU8230), Hitachi, Japan] and transmission electron microscope (Tecnai G² F30 S-TWIN, FEI, USA).

Gas Sensing Tests: The sensor devices were mounted on a custom-made testing chamber and connected to a dual-channel current sourcemeter (2636b, Keithley, USA) to apply forward bias on a μLPs and measure the sensing resistance. Gas was supplied to the sensor device, and the concentration of NO_2 gas was adjusted by controlling the flow rates of NO_2 gas and dry air ($\approx 0\%$ relative humidity) with mass flow controllers. For evaluating sensor responses in various temperature conditions, pristine In_2O_3 , Ag NP-coated In_2O_3 , and Pt-NP-coated In_2O_3

were prepared on gold interdigitated electrodes patterned on quartz pieces (size $= 1 \times 1 \text{ cm}^2$). Electrically wired samples were mounted on a tube furnace system (Lindberg Blue M, Thermo Fisher Scientific, USA) and heated up to 100 – 250°C during the NO_2 gas test. The electrical resistance of each sensing material was measured with a current sourcemeter (2636b, Keithley, USA).

Supporting Information

Supporting Information is available from the Wiley Online Library or from the author.

Acknowledgements

This work was supported by the Multi-Ministry Collaborative R&D Program (Development of Techniques for Identification and Analysis of Gas Molecules to Protect against Toxic Substances) through the National Research Foundation of Korea (NRF) funded by KNPA, MSIT, MOTIE, ME, and NFA (Grant No. NRF-2022M3D9A1023618), and by the National Research Foundation of Korea (NRF) grant funded by the Korean government (MSIT) (NRF-2021R1A2C3008742).

Conflict of Interest

The authors declare no conflict of interest.

Author Contributions

I.C., Y.C.S., and K.L. contributed equally to this work. I.C., Y.C.S., and K.L. planned and conducted the experiments and wrote the paper. M.C. contributed to the design of sensor devices. J.P. and M.K. contributed to fabrication and characterization of sensor devices. K.S.C. and C.B.J. contributed to the experiments and analysis for characterizing surface temperature of the sensor devices. Y.H.C. and I.P. supervised the project. All the authors worked on the paper.

Data Availability Statement

Research data are not shared.

Keywords

metal oxide nanomaterials, micro light-emitting diodes (LEDs), plasmonics, ultra-low power gas sensors

Received: November 18, 2022

Revised: February 3, 2023

Published online: March 28, 2023

- [1] P. Bhattacharyya, *IEEE Trans. Device Mater. Reliab.* **2014**, *14*, 589.
- [2] Q. Zhou, A. Sussman, J. Chang, J. Dong, A. Zettl, W. Mickelson, *Sens. Actuator A Phys.* **2015**, *223*, 67.
- [3] K. Kang, D. Yang, J. Park, S. Kim, I. Cho, H.-H. Yang, M. Cho, S. Mousavi, K. H. Choi, I. Park, *Sens. Actuators, B* **2017**, *250*, 574.
- [4] I. Cho, K. Kang, D. Yang, J. Yun, I. Park, *ACS Appl. Mater. Interfaces* **2017**, *9*, 27111.

- [5] K.-W. Choi, J.-S. Lee, M.-H. Seo, M.-S. Jo, J.-Y. Yoo, G. S. Sim, J.-B. Yoon, *Sens. Actuators, B* **2019**, 289, 153.
- [6] A. Rao, H. Long, A. Harley-Trochimczyk, T. Pham, A. Zettl, C. Carraro, R. Maboudian, *ACS Appl. Mater. Interfaces* **2017**, 9, 2634.
- [7] H. Long, A. Harley-Trochimczyk, T. He, T. Pham, Z. Tang, T. Shi, A. Zettl, W. Mickelson, C. Carraro, R. Maboudian, *ACS Sens.* **2016**, 1, 339.
- [8] Y. Lim, S. Lee, Y. M. Kwon, J. M. Baik, H. Shin, presented at 2018 IEEE Micro Electro Mechanical Systems (MEMS), Belfast, UK, January **2018**.
- [9] G. Meng, F. Zhuge, K. Nagashima, A. Nakao, M. Kanai, Y. He, M. Boudot, T. Takahashi, K. Uchida, T. Yanagida, *ACS Sens.* **2016**, 1, 997.
- [10] J. Prades, R. Jimenez-Diaz, F. Hernandez-Ramirez, S. Barth, A. Cirera, A. Romano-Rodriguez, S. Mathur, J. Morante, *Appl. Phys. Lett.* **2008**, 93, 123110.
- [11] J. H. Ahn, J. Yun, D. I. Moon, Y. K. Choi, I. Park, *Nanotechnology* **2015**, 26, 095501.
- [12] J. Yun, C. Y. Jin, J. H. Ahn, S. Jeon, I. Park, *Nanoscale* **2013**, 5, 6851.
- [13] L. Zhu, W. Zeng, *Sens. Actuator A Phys.* **2017**, 267, 242.
- [14] J. Zhang, X. Liu, G. Neri, N. Pinna, *Adv. Mater.* **2016**, 28, 795.
- [15] F. Mendoza, D. M. Hernández, V. Makarov, E. Febus, B. R. Weiner, G. Morell, *Sens. Actuators, B* **2014**, 190, 227.
- [16] J. H. Kim, J. Chun, J. W. Kim, W. J. Choi, J. M. Baik, *Adv. Funct. Mater.* **2015**, 25, 7049.
- [17] M. H. Seo, K. Kang, J. Y. Yoo, J. Park, J. S. Lee, I. Cho, B. J. Kim, Y. Jeong, J. Y. Lee, B. Kim, J. Rho, J. B. Yoon, I. Park, *ACS Nano* **2020**, 14, 16813.
- [18] J. Jang, K. Kang, N. Raeis-Hosseini, A. Ismukhanova, H. Jeong, C. Jung, B. Kim, J. Y. Lee, I. Park, J. Rho, *Adv. Opt. Mater.* **2020**, 8, 1901932.
- [19] K. Kang, J. Park, B. Kim, K. Na, I. Cho, J. Rho, D. Yang, J. Y. Lee, I. Park, *ACS Appl. Mater. Interfaces* **2020**, 12, 39024.
- [20] C. Y. Wang, V. Cimalla, T. Kups, C. C. Röhlig, T. Stauden, O. Ambacher, M. Kunzer, T. Passow, W. Schirmacher, W. Pletschen, K. Köhler, J. Wagner, *Appl. Phys. Lett.* **2007**, 91, 103509.
- [21] O. Casals, N. Markiewicz, C. Fabrega, I. Gracia, C. Cane, H. S. Wasisto, A. Waag, J. D. Prades, *ACS Sens.* **2019**, 4, 822.
- [22] S. Zhang, H. Li, X. Wang, Y. Liu, J. Dai, C. Chen, *ACS Omega* **2020**, 5, 9985.
- [23] I. Cho, Y. C. Sim, M. Cho, Y. H. Cho, I. Park, *ACS Sens.* **2020**, 5, 563.
- [24] R. Jaaniso, O. K. Tan, *Semiconductor gas sensors*, 1st ed., Woodhead Publishing Limited, Swastan, Cambridge, UK, **2013**.
- [25] M. W. Knight, Y. Wang, A. S. Urban, A. Sobhani, B. Y. Zheng, P. Nordlander, N. J. Halas, *Nano Lett.* **2013**, 13, 1687.
- [26] C. Clavero, *Nat. Photonics* **2014**, 8, 95.
- [27] M. W. Knight, H. Sobhani, P. Nordlander, N. J. Halas, *Science* **2011**, 332, 702.
- [28] M. Moskovits, *Science* **2011**, 332, 676.
- [29] K. Robbie, J. Sit, M. Brett, *J. Vac. Sci. Technol* **1998**, 16, 1115.
- [30] K. S. Chang, S. C. Yang, J. Y. Kim, M. H. Kook, S. Y. Ryu, H. Y. Choi, G. H. Kim, *Sensors* **2012**, 12, 4648.
- [31] A. Walsh, J. L. Da Silva, S. H. Wei, *J Phys Condens Matter* **2011**, 23, 334210.
- [32] D. Gall, *J. Appl. Phys.* **2016**, 119, 085101.
- [33] X. C. Ma, Y. Dai, L. Yu, B. B. Huang, *Light Sci Appl* **2016**, 5, e16017.
- [34] D. Kim, D. Yang, K. Kang, M. A. Lim, Z. Li, C.-O. Park, I. Park, *Sens. Actuators, B* **2016**, 226, 579.
- [35] A. P. Lee, B. J. Reedy, *Sens. Actuators, B* **1999**, 60, 35.
- [36] G. Korotcenkov, I. Boris, V. Brinzari, S. Han, B. Cho, *Sens. Actuators, B* **2013**, 182, 112.
- [37] S. Ahlers, G. Müller, T. Doll, *Encycl. Sens.* **2006**, 3, 413.
- [38] J. D. Prades, R. Jimenez-Diaz, M. Manzanares, F. Hernandez-Ramirez, A. Cirera, A. Romano-Rodriguez, S. Mathur, J. R. Morante, *Phys. Chem. Chem. Phys.* **2009**, 11, 10881.
- [39] A. Shrivastava, V. Gupta, *Chron. Young Sci.* **2011**, 2, 21.
- [40] B. Gong, T. Shi, W. Zhu, G. Liao, X. Li, J. Huang, T. Zhou, Z. Tang, *Sens. Actuators, B* **2017**, 245, 821.
- [41] C.-L. Hsu, L.-F. Chang, T.-J. Hsueh, *Sens. Actuators, B* **2017**, 249, 265.
- [42] M. Kang, I. Cho, J. Park, J. Jeong, K. Lee, B. Lee, D. V. Del Orbe, K. Yoon, I. Park, *ACS Sens.* **2022**, 7, 430.
- [43] T. Kim, W. Cho, B. Kim, J. Yeom, Y. M. Kwon, J. M. Baik, J. J. Kim, H. Shin, *Small* **2022**, 18, 2204078.